High catalytic activity for formaldehyde oxidation of an interconnected network structure composed of δ-MnO$_2$ nanosheets and γ-MnOOH nanowires

Ying Tao[1,2] · Rong Li[1,3] · Ai-Bin Huang[1] · Yi-Ning Ma[4] · Shi-Dong Ji[2] · Ping Jin[1] · Hong-Jie Luo[2]

Abstract Among the transition metal oxide catalysts, manganese oxides have great potential for formaldehyde (HCHO) oxidation at ambient temperature because of their high activity, nontoxicity, low cost, and polybasic morphologies. In this work, a MnO$_2$-based catalyst (M-MnO$_2$) with an interconnected network structure was successfully synthesized by a one-step hydrothermal method. The M-MnO$_2$ catalyst was composed of the main catalytic agent, δ-MnO$_2$ nanosheets, dispersed in a nonactive framework material of γ-MnOOH nanowires. The catalytic activity of M-MnO$_2$ for HCHO oxidation at room temperature was much higher than that of the pure δ-MnO$_2$ nanosheets. This is attributed to the special interconnected network structure. The special interconnected network structure has high dispersion and specific surface area, which can provide more surface active oxygen species and higher surface hydroxyl groups to realize rapid decomposition of HCHO.

Keywords MnO$_2$ · Formaldehyde · Catalytic oxidation · Hydrothermal synthesis

✉ Rong Li
lirong@mail.sic.ac.cn

✉ Shi-Dong Ji
sdki@mail.sic.ac.cn

1 State Key Laboratory of High Performance Ceramics and Superfine Microstructure, Shanghai Institute of Ceramics, Chinese Academy of Sciences, Shanghai 200050, People's Republic of China

2 Institute for the Conservation of Culture Heritage, Shanghai University, Shanghai 200444, People's Republic of China

3 University of Chinese Academy of Sciences, Beijing 100049, People's Republic of China

4 Department of Criminal Science and Technology, Jiangsu Police Institute, Nanjing 210031, People's Republic of China

1 Introduction

Formaldehyde (HCHO) is a typical indoor air pollutant that is mainly released from furnishings and building materials [1–3]. Long-term exposure to HCHO can induce adverse health consequences, such as allergic rhinitis, asthma, respiratory system diseases, hepatitis, pneumonia, nasopharyngeal cancer, and leukemia [4–7]. In previous studies, several approaches for HCHO oxidation have been developed, such as biological degradation, photocatalytic oxidation, adsorption, and thermal catalytic oxidation. It has been proved that room-temperature catalytic oxidation is one of the most promising and cost-effective methods for high-efficiency conversion of HCHO into harmless species (H$_2$O, CO$_2$) over a metal oxide catalyst [8–10].

Noble metal catalysts, mainly containing Pt, Au, Pd, and Ag as the active component supported on various metal oxides (TiO$_2$, Al$_2$O$_3$, ZrO$_2$, and Fe$_2$O$_3$), show high performance for HCHO oxidation at ambient temperature [11–14]. However, their high cost, poor thermal stabilities, and limited resources have prevented a wide application of noble metal catalysts. It was found that transition metal oxide catalysts had enormous potential for HCHO oxidation at room temperature. In particular, the transition metal oxide catalysts such as MnO$_x$, Co$_3$O$_4$, and CeO$_2$ show good thermal stability and are less expensive and more abundant than noble metal catalysts [15–18].

Among the transition metal oxide catalysts, manganese oxides have been widely used in catalysis because of their high activity, nontoxicity, low cost, polybasic structures, and morphologies [10–22]. The structures of manganese oxide, including α-MnO$_2$, β-MnO$_2$, γ-MnO$_2$, and δ-MnO$_2$, play an important role in catalytic capacity [23–27]. Zhang et al. [25] found that δ-MnO$_2$ had the highest activity because of its special 2D layer tunnel structure that

contained the most active oxygen species and the highest amount of lattice oxygen species on the catalyst surface. Birnessite (δ-MnO$_2$) [23, 25] is a layered manganese dioxide constructed by an edge-sharing [MnO$_6$] octahedra framework with a certain number of cations (Li$^+$, Na$^+$, Ca^{2+}) and water molecules located between the manganese oxide layers for charge balance. Wang et al. [17] found that the water content in the birnessite was essential for HCHO oxidation—that was, better activity was obtained for materials with higher water content. They also found that the HCHO oxidation efficiency was influenced by the different types of interlayer cation (K$^+$, Mg^{2+}, Ca^{2+}, Fe^{3+}) [18, 19]. However, the agglomeration of the nanosheets in δ-MnO$_2$ can reduce the exposed active sites. In the past few years, MnO$_2$ has usually been supported on carbon materials (graphene hydrogel, carbon foam, carbon nanotubes, and carbon fibers) to solve the problem of agglomeration [28, 29]. However, these carbon materials are inert components in catalysts and may cover the active sites for catalytic reactions. To solve this problem, Rong et al. [30, 31] developed an organic and template-free approach to prepare 3D MnO$_2$ by freeze-drying aqueous solutions of the MnO$_2$ nanosheets and nanowires. Although improved catalytic performance was obtained, this method involved multiple steps and was cumbersome.

In this report, a one-step hydrothermal method for the fabrication of a MnO$_2$-based catalyst (M-MnO$_2$) composed of δ-MnO$_2$ nanosheets anchored on a nanowire-shaped γ-MnOOH framework is described. It exhibits high performance for HCHO oxidation at room temperature.

2 Experimental

2.1 Catalyst preparation

All the chemicals used in this study were of analytical grade, and deionized water was used for all preparations. KMnO$_4$ and (NH$_4$)$_2$C$_2$O$_4$·H$_2$O were purchased from Sinopharm Chemical Reagent Co., Ltd. Deionized water was obtained from a highly pure water system (Thermo Co., USA).

The catalysts were synthesized by a facile redox reaction through the hydrothermal method. A series of reactions for different MnO$_2$ structures were carried out by changing the dosage of the reducing agent. Typically, KMnO$_4$ (6.33 mmol) and (NH$_4$)$_2$C$_2$O$_4$·H$_2$O (2.81, 5.98 and 11.26 mmol) were mixed with deionized water (40 mL) under vigorous stirring at room temperature. Then, the solution was transferred into a 100-mL Teflon-lined stainless-steel autoclave maintained at 100 °C for 10 h at a heating rate of 5 °C/min in an electric oven. Then, the autoclave was cooled to room temperature, and the precipitate was collected by centrifugal separation, washed three times with distilled water and ethanol, and dried in vacuum at 80 °C for 12 h.

2.2 Characterization

The catalysts were characterized using an X-ray diffractometer (D8 ADVANCE, Bruker, Germany) operated at 40 kV and 40 mA with Cu-K$_\alpha$ radiation (λ = 0.154 2 nm) at a scanning rate of 5 °/min in the 2θ range of 5°–80°. The morphology and microstructure of the samples were determined using a Magellan 400 field-emission scanning electron microscope (FE-SEM, USA) and a Tecnai G2 F20 transmission electron microscope (TEM, Netherlands). X-ray photoelectron spectroscopy (XPS) measurements were performed using an ESCALAB 250 X-ray photoelectron spectrometer (Thermo Fisher, UK) microprobe with an Al-K$_\alpha$ source (λ = 1 486.7 eV) at a pass energy of 30 eV. The XPSPEAK41 peak fitting program was applied to fit the Mn 2p$_{3/2}$, Mn 2p$_{1/2}$, and O 1s spectra. The specific surface area and the pore volume of the samples were determined by the multipoint Brunauer-Emmett-Teller method and Barrett-Joyner-Halenda analyses.

Hydrogen temperature-programmed reduction (H$_2$-TPR) and oxygen temperature-programmed desorption (O$_2$-TPD) were performed using a Chemisorb 2920 instrument (USA) with a thermal conductivity detector (TCD). For H$_2$-TPR, the sample (50 mg) was first pretreated with He (30 mL/min) at 150 °C for 1 h and then cooled to room temperature. Next, the temperature was increased from 25 °C to 600 °C at a heating rate of 5 °C/min with a flow of 5% H$_2$/Ar at a flow rate of 30 mL/min that passed the samples monitored by the TCD. For O$_2$-TPD, the sample (50 mg) was first pretreated with He (30 mL/min) at 300 °C for 30 min to remove physically adsorbed and interlayer H$_2$O and surface oxygen, and then it was cooled to room temperature with flowing O$_2$ for 30 min. Next, the sample was purged with He for 1 h to remove the weakly adsorbed O$_2$. Finally, the temperature was increased from room temperature to 500 °C at a heating rate of 10 °C/min under He flow (30 mL/min). In situ diffuse reflectance infrared Fourier transform spectroscopy (DRIFTS) was performed using a Fourier transform infrared spectrometer (Nicolet 6700, Thermo Fisher, USA) to identify the intermediate species during HCHO oxidation. All spectra were measured with a resolution of 4 cm^{-1} and an accumulation of 32 scans. Prior to exposure to HCHO flowing gas, the samples were pretreated by He (30 mL/min) for 30 min at room temperature. Then, the reactant gas mixture (80 mg/kg of HCHO/N$_2$ + 20% O$_2$/N$_2$) was injected into the DRIFTS cell at a flow rate of 60 mL/min. Before the data were recorded, the samples were swept by He (30 mL/min) for 1 min to remove weakly adsorbed species.

2.3 Catalytic activity tests

The evaluation of the catalytic activity system hast two parts: static and dynamic experiments.

For static experiments, the catalytic activities of different samples were evaluated in a 5-L glass reactor at room temperature. A small electric fan (0.5 W) was securely fixed on the top of the reactor to ensure the uniform dispersal of the HCHO gas. The temperature of the glass reactor was maintained at 25 °C during the reaction. Moreover, the relative humidity inside the reactor was controlled to 60%, which was close to the environmental humidity. Typically, the sample (100 mg) was spread on a watch glass that was placed at the bottom of the glass reactor, and then HCHO solution (38%, 15 μL) was injected into the reactor. The initial concentration of HCHO gas was 180 mg/kg when the HCHO solution was volatilized completely and then was analyzed by the 3-methyl-2-benzothiazolinone hydrazine method.

For the dynamic experiments, HCHO oxidation was performed in a fixed bed reactor under atmospheric pressure within a temperature range of 25–180 °C. The sample (100 mg) was placed in a quartz tube with a diameter of 6 mm that was used as the reactor. The temperature of the reactor was controlled using a constant temperature controller. HCHO gas was generated by flowing compressed air (21% O_2) over the paraformaldehyde in a water bath at 25 °C at a flow rate of 100 mL/min. The inlet concentration of HCHO was 100 mg/kg, corresponding to a gas hourly space velocity (GHSV = 60 000 mL/(g_{cat} ·h).

For kinetics measurements, the HCHO conversion was controlled to be < 15%. The reaction rate (v) was calculated from the dynamic experiments according to

$$v\left(mol/(s \cdot g_{cat})\right) = \frac{C_{HCHO}F_{gas}\eta}{m_{cat}}, \tag{1}$$

where C_{HCHO} is the HCHO concentration of the feed gas (mol/mL), F_{gas} the total flow rate during HCHO oxidation, η the stable HCHO conversion, and m_{cat} the mass of the catalyst in the reactor bed.

To calculate the apparent activation energy (E_a), it is assumed that HCHO oxidation follows the first-order reaction kinetics. According to the Arrhenius formula, the obtained kinetic model can be described by

$$\ln v = -\frac{E_a}{RT} - \ln k_0 + \ln C_{HCHO}, \tag{2}$$

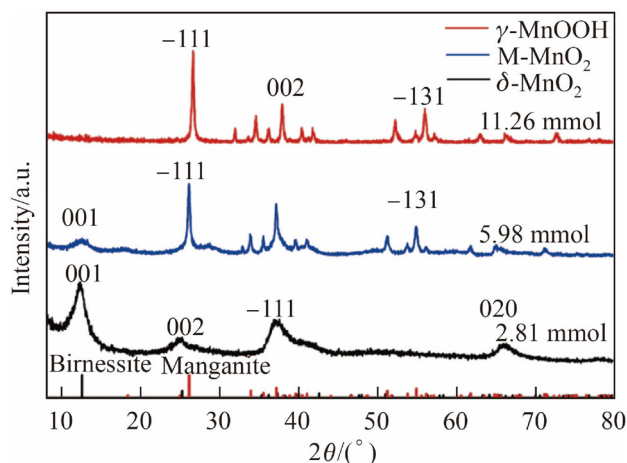where R is the molar gas constant, T the catalytic temperature, k_0 the reaction constant.

Fig. 1 XRD patterns of δ-MnO$_2$, M-MnO$_2$ and γ-MnOOH

3 Results and discussion

Figure 1 shows the X-ray diffraction (XRD) patterns of the as-synthesized samples. As 2.81 mmol (NH$_4$)$_2$C$_2$O$_4$ was added, all peaks of the sample could be indexed to the birnessite (JCPDS No. 80-1098); thereafter, it was named "δ-MnO$_2$". With the increase of (NH$_4$)$_2$C$_2$O$_4$ (5.98 mmol), the final product was a mixed phase (named "M-MnO$_2$") of δ-MnO$_2$ and manganite γ-MnOOH (JCPDS No. 88-0649). After more reductants (11.26 mmol) were added, the birnessite phase disappeared, and there was only manganite; therefore, the sample was named "γ-MnOOH" [32, 33]. The wide peak widths of birnessite in δ-MnO$_2$ and M-MnO$_2$ indicate poor crystallinity, which may be caused by the damage to the ordered structure.

The morphology and microstructure of these three samples were observed using SEM and TEM, as shown in Fig. 2. The morphology of γ-MnOOH nanowires can be observed clearly in Figs. 2a, d, and g, and the nanowires are randomly intertwined. The particles reveal a nanorod like morphology with a width of less than 50 nm and a length of approximately 1 μm, and the lattice fringes of 0.48 nm can be assigned to the (100) planes. The particles shown in Figs. 2b, e, and h are δ-MnO$_2$. Figure 2b shows a flowerlike structure comprising nanoparticles, and the size of the nanoparticles observed in Fig. 2h is approximately 5–10 nm. The distances between the adjacent lattice fringes are 0.24 nm and 0.35 nm, which are related to the (−111) and (002) planes, respectively. However, the particles of the flowerlike structure in Fig. 2b show severe agglomeration. As shown in Figs. 2c, f, and i, M-MnO$_2$ shows a special interconnected network structure with the flowerlike δ-MnO$_2$ anchored on the γ-MnOOH nanowires. The γ-MnOOH as a framework support plays an essential role in the network structure, and δ-MnO$_2$ is dispersed on the framework. The distances between the adjacent lattice
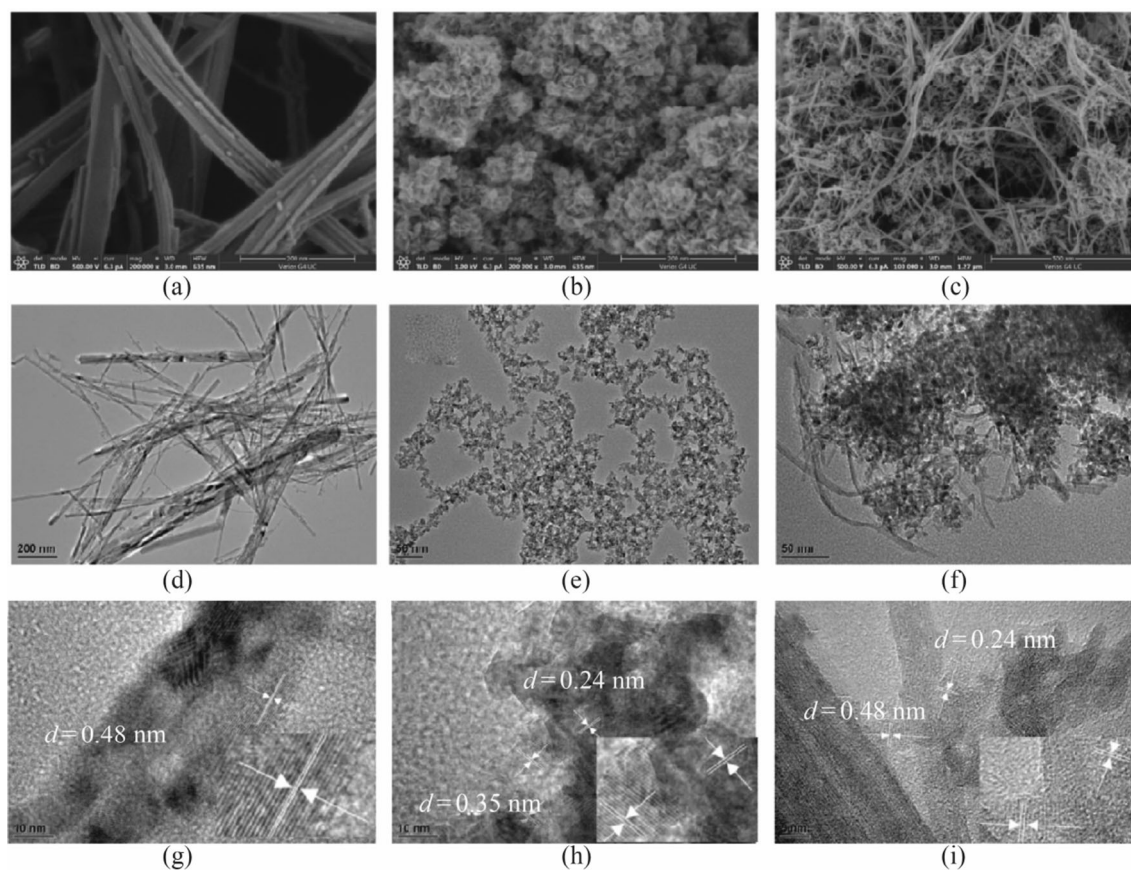
Fig. 2 SEM, TEM and high resolution TEM images of different samples **a, d, g** γ-MnOOH, **b, e, h** δ-MnO$_2$, and **c, f, i** M-MnO$_2$ (the insets show the amplifying TEM images of the samples)

fringes of M-MnO$_2$ were 0.24 nm and 0.48 nm for δ-MnO$_2$ and γ-MnOOH, respectively. It was concluded that the sample with this special morphology was a mixture of δ-MnO$_2$ and γ-MnOOH. This is also supported by the XRD results. The morphology of the as-synthesized products can be regulated by modulating the ratio of (NH$_4$)$_2$C$_2$O$_4$/KMnO$_4$ during the hydrothermal process. With the increase of the ratio of (NH$_4$)$_2$C$_2$O$_4$/KMnO$_4$, the low-valent manganese compound γ-MnOOH appeared. The δ-MnO$_2$ nanosheets tended to anchor on a nanowire-shaped γ-MnOOH, which increased the specific surface area and the pore volume compared with the pure δ-MnO$_2$, as shown in Table 1.

For the case in which the main catalyst is δ-MnO$_2$, XPS measurements are performed to analyze the surface chemical compositions and the valence state of γ-MnOOH, δ-MnO$_2$, and M-MnO$_2$, and the results are shown in Figs. 3a and b. The Mn 2p$_{3/2}$ peak can be deconvoluted into two peaks, located at 641.1–641.2 eV and 642.4–642.7 eV that correspond to the Mn^{3+} and Mn^{4+} species, respectively. The Mn^{4+}/Mn^{3+} ratios of γ-MnOOH (0.85), δ-MnO$_2$ (1.71), and M-MnO$_2$ (1.18) are calculated from the XPS data by their peak area ratios and are summarized in Table 1. The Mn^{4+}/Mn^{3+} ratios were in the order δ-MnO$_2$ > M-MnO$_2$ > γ-MnOOH.

Table 1 Component analysis of γ-MnOOH, δ-MnO$_2$ and M-MnO$_2$

Catalysts	Binding energy/eV		Mn^{4+}/Mn^{3+}	Binding energy/eV		O$_{ads}$/O$_{latt}$	BET/(m$^2 \cdot$ g^{-1})	Pore volume/(cm$^3 \cdot$ g^{-1})
	Mn^{4+}	Mn^{3+}		O$_{ads}$	O$_{latt}$			
γ-MnOOH	642.7	641.2	0.85	531.4	529.7	0.46	126.4	0.224
δ-MnO$_2$	642.6	641.1	1.71	531.3	529.8	0.53	21.7	0.076
M-MnO$_2$	642.4	641.1	1.18	531.4	529.8	0.62	98.1	0.197
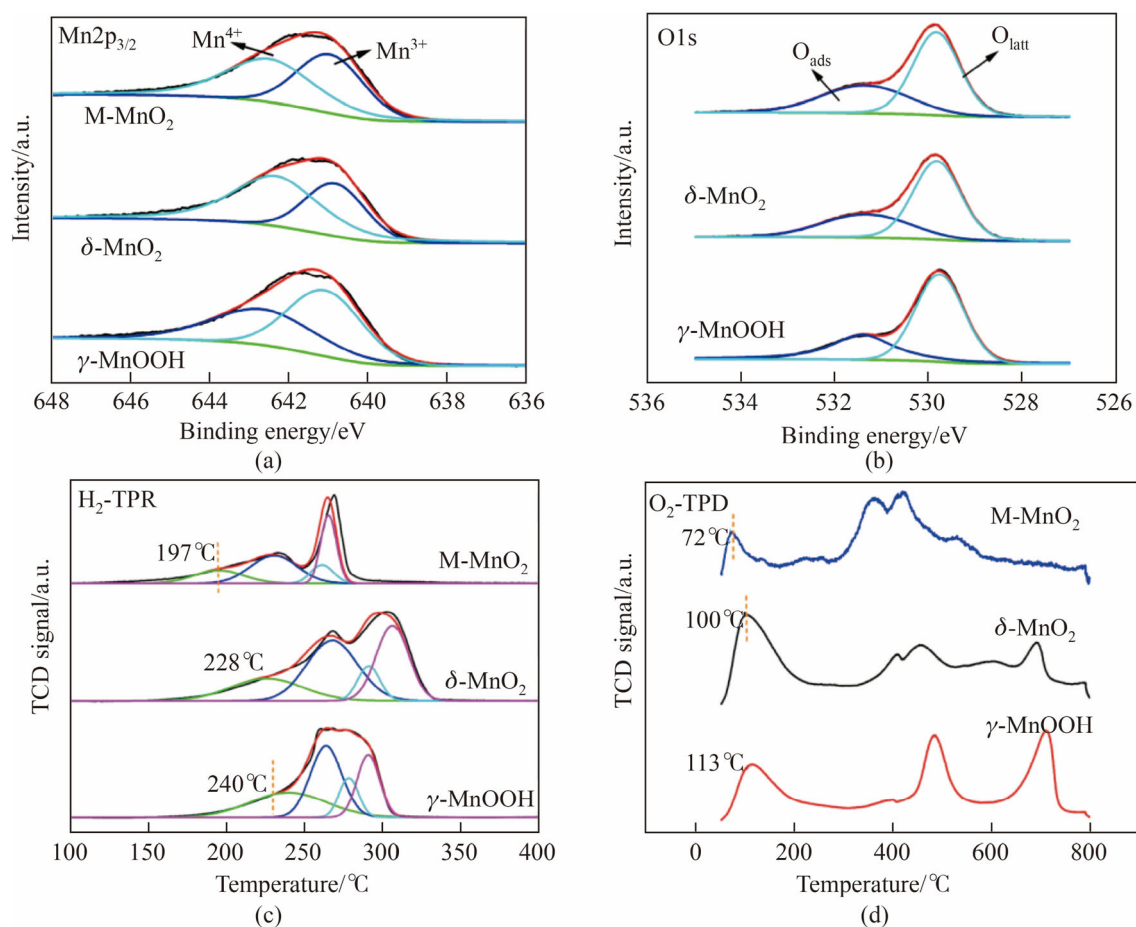
Fig. 3 **a** Mn 2p and **b** O 1s XPS spectra of γ-MnOOH, δ-MnO$_2$ and M-MnO$_2$, **c** H$_2$-TPR and **d** O$_2$-TPD of the γ-MnOOH, δ-MnO$_2$ and M-MnO$_2$

In addition, as shown in Fig. 3b, the O 1s spectra of the three different samples were deconvoluted into two peaks located at 529.9 eV and 531.4 eV that were associated with lattice oxygen (O$_{latt}$) and surface adsorbed oxygen (O$_{ads}$) species, respectively. The O$_{ads}$/O$_{latt}$ ratios of the three samples are calculated from the XPS data using their peak area ratios and are presented in Table 1. The O$_{ads}$/O$_{latt}$ ratio of M-MnO$_2$ was 0.62, while that of δ-MnO$_2$ was 0.53 and that of γ-MnOOH was 0.46. The O$_{ads}$/O$_{latt}$ ratios followed the order M-MnO$_2$ > δ-MnO$_2$ > γ-MnOOH. The M-MnO$_2$ surface has the most-abundant surface adsorbed oxygen, which is mainly present in the form of active oxygen species, such as $\cdot$O$_2^-$ and $\cdot$O$^-$ [34]. Previous studies have shown that the catalytic oxidation activity at low temperatures is closely related to the content of surface oxygen species, and most of the O$_{ads}$ is generated from the adsorption and activation of adsorbed oxygen at oxygen vacancies [31]. The highest O$_{ads}$/O$_{latt}$ ratios are ascribed to the high-specific-surface area and can expose more active sites, which can be deduced from the SEM images and higher-surface-area data.

H$_2$-TPR experiments were performed to investigate the reducibility of the three samples. Figure 3c shows the H$_2$-TPR profiles of γ-MnOOH, δ-MnO$_2$, and M-MnO$_2$ catalysts with increasing temperature that can be deconvoluted into four peaks, named peaks 1, 2, 3, and 4. Among these, the peak area ratio of peaks 2, 3, and 4 is approximately 3:1:2 for all samples. This can be associated with the sequential reduction of MnO$_2$ to Mn$_2$O$_3$, Mn$_2$O$_3$ to Mn$_3$O$_4$, and Mn$_3$O$_4$ to MnO [28]. However, the first reduction peaks for γ-MnOOH, δ-MnO$_2$, and M-MnO$_2$ are located at 240 °C, 228 °C, and 197 °C, respectively. M-MnO$_2$ showed the lowest initial reduction temperature among all of the samples, suggesting that its surface oxygen species showed the highest reducibility and activity. It is clear that the highest oxidation potential is in the order of M-MnO$_2$ > δ-MnO$_2$ > γ-MnOOH, which is consistent with the results for the catalytic activity of HCHO oxidation by these samples.

O$_2$-TPD experiments were performed to investigate the activity of the surface adsorbed oxygen in different samples. Several O$_2$ desorption peaks were observed from in the 40–500 °C, as shown in Fig. 3d. The first desorption

peak was assigned to the surface adsorbed oxygen ($\cdot O_2^-$/ $\cdot O^-$), while the rest of the peaks were related to the release of lattice oxygen [35, 36]. The first surface adsorbed oxygen desorption occurred at temperatures of 113 °C, 100 °C, and 72 °C for γ-MnOOH, δ-MnO$_2$, and M-MnO$_2$, respectively. M-MnO$_2$ showed the lowest surface adsorbed oxygen desorption temperature, indicating that the surface adsorbed oxygen of M-MnO$_2$ exhibited the highest mobility and activity. Furthermore, the special interconnected network structure of M-MnO$_2$ favors mass transfer and exposes more active sites.

The specific surface area and pore volume of γ-MnOOH, δ-MnO$_2$, and M-MnO$_2$ are shown in Table 1. The specific surface area and the pore volume of γ-MnOOH were higher than those of the other two species, and those of δ-MnO$_2$ were the lowest. This was because of the high dispersion of γ-MnOOH nanowires and the severe agglomeration of δ-MnO$_2$ nanosheets. M-MnO$_2$ has a special structure composed of δ-MnO$_2$ nanoparticles anchored on nanowire-shaped γ-MnOOH, which avoids the severe agglomeration of δ-MnO$_2$.

The catalytic activities of γ-MnOOH, δ-MnO$_2$, and M-MnO$_2$ for HCHO removal at room temperature are compared in Fig. 4. For the static experiment, shown in Fig. 4a, the concentration of HCHO was decreased from 180 to 142, 80 and 34 mg/kg within 1 h by γ-MnOOH, δ-MnO$_2$, and M-MnO$_2$, respectively. In the static catalytic activity test, M-MnO$_2$ showed significantly higher HCHO removal ability than the other samples, and the catalytic efficiency of γ-MnOOH was quite low. The test demonstrated that δ-MnO$_2$ was the main active component for HCHO oxidation in the M-MnO$_2$ catalyst.

The dynamic experiment results further illustrate the catalytic activities of the different samples, as shown in Fig. 4b. The catalytic efficiencies of γ-MnOOH, δ-MnO$_2$, and M-MnO$_2$ were 4%, 36%, and 53% at room temperature, respectively. Meanwhile, T_{100} refers to the temperature of complete HCHO conversion. The T_{100} of γ-MnOOH, δ-MnO$_2$, and M-MnO$_2$ were 160 °C, 120 °C, and 90 °C, respectively. This shows that the γ-MnOOH catalyst needs a tremendous amount of energy (160 °C) to achieve complete HCHO conversion. The three catalysts' variation tendency in Fig. 4b is similar to that of the static
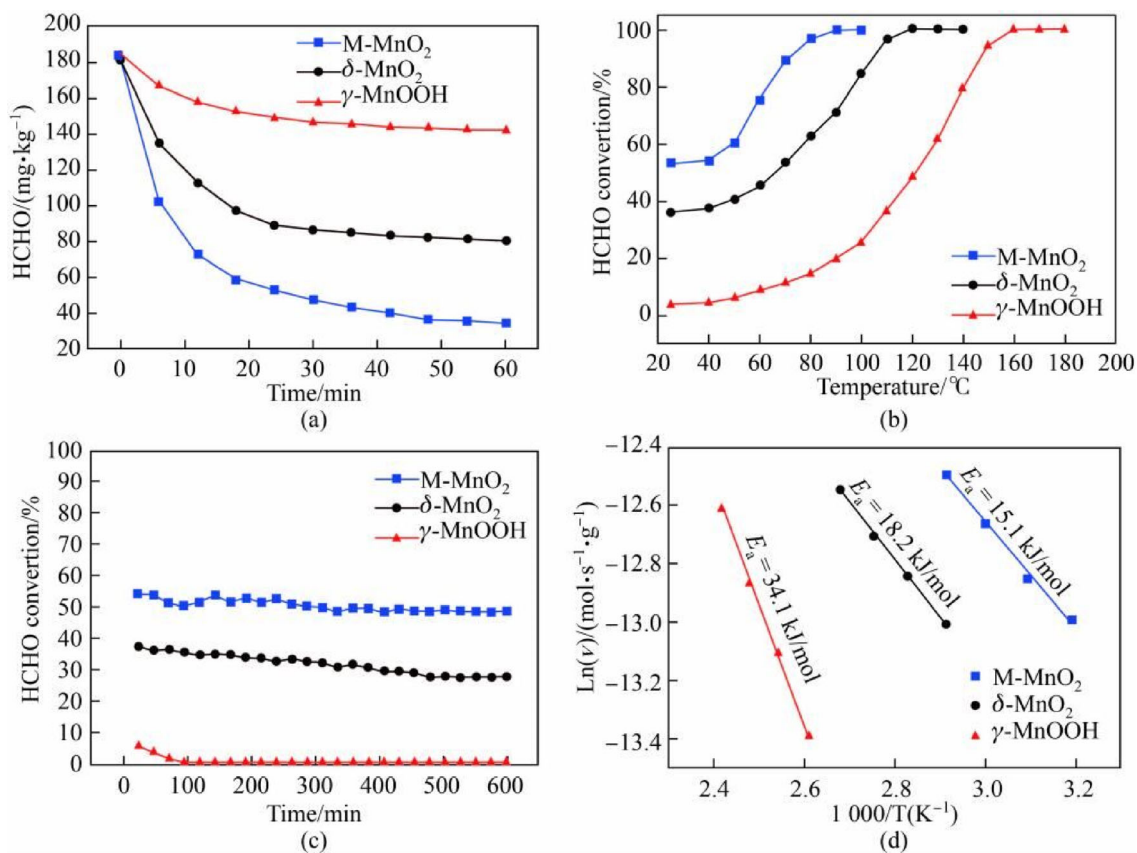

Fig. 4 **a** Changes in the HCHO concentration with the catalytic time at room temperature in the static experiments, **b** HCHO conversion with the rise of temperature over the different MnO$_2$ catalysts in the dynamic experiments, **c** stability test of the different MnO$_2$ catalysts at room temperature in the dynamic experiments and **d** Arrhenius plots for HCHO oxidation for the different MnO$_2$ catalysts

experiments in Fig. 4a. The order of the catalytic efficiency is M-MnO$_2$ > δ-MnO$_2$ > γ-MnOOH.

The catalytic stability and HCHO removal efficiency are important for the practical applications of the catalysts [34]. Therefore, the catalytic HCHO removal efficiencies of the three samples were tested in a series of relatively long-term experiments, as shown in Fig. 4c. The catalytic efficiency of M-MnO$_2$ was greater than 50% and remained stable during the entire 10 h test. Meanwhile, the HCHO removal efficiency of pure δ-MnO$_2$ decreased sharply from 36% to 27% within 10 h, while that of pure γ-MnOOH was initially 6% and then rapidly decreased to zero. These results further indicate that the catalytic efficiency of M-MnO$_2$ is higher than that of the other two catalysts and can be maintained for a long time at room temperature.

The apparent activation energies (E_a) of the three samples are given in Fig. 4d and were calculated according to the Arrhenius plots of the catalysts for HCHO oxidation. The E_a values for γ-MnOOH, δ-MnO$_2$, and M-MnO$_2$ were 34.1, 18.2 and 15.1 kJ/mol, respectively. It is clear that HCHO is oxidized more easily by M-MnO$_2$ because it has a lower E_a value than γ-MnOOH and δ-MnO$_2$.

Thermogravimetry (TG) analysis was used for evaluating the weight loss and qualitative analysis for detachable species in different samples with increasing temperature (see Fig. 5). Mass spectral analysis was used to confirm the detachable species according to mass charge ratio (m/z). It was found that the m/z of all detachable species was close to 18, which was consistent with the water molecule. The content of the largest surface adsorbed water loss (less than 100 °C) was 9.21% for M-MnO$_2$, followed by δ-MnO$_2$ and γ-MnOOH, which were only 3.68% and 2.71%, respectively. According to the literature, the surface adsorbed water can provide a rich surface hydroxyl group, which promotes the efficiency of HCHO oxidation at room temperature [17].
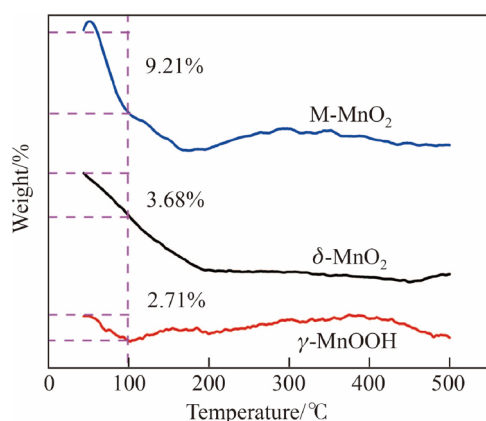

Fig. 5 Thermogravimetry (TG) curves of the γ-MnOOH, δ-MnO$_2$ and M-MnO$_2$

To explain why the M-MnO$_2$ catalyst shows excellent catalytic activity and to observe the reaction process and mechanism, in situ DRIFTS spectra of the three samples exposed in the 80 mg/kg HCHO/N$_2$ + 20% O$_2$/N$_2$ for HCHO oxidation at room temperature were obtained (see Fig. 6). There was no obvious material change on the surface of γ-MnOOH, which indicated that the catalytic reaction was weak. The material change on the surface of δ-MnO$_2$ and M-MnO$_2$ was obvious, which also confirmed that δ-MnO$_2$ was the main catalytic agent, and the catalyst activity of γ-MnOOH could be ignored at room temperature. The band at 1 465 cm^{-1} represents the dioxymethylene (DOM) species ($δ(CH_2)$), suggesting that HCHO first absorbed on the samples to form DOM because the carbonyl carbon in HCHO is electrophilic and tends to adsorb on the nucleophilic surface oxygen atom. The weak intensity of the DOM band indicates that DOM can be rapidly transformed into formate species with surface oxygen. Moreover, the band at 1 465 cm^{-1} is much lower in the M-MnO$_2$ sample, suggesting that the DOM on M-MnO$_2$ can be decomposed faster than that on a pure δ-MnO$_2$ sample.

Formate species are the well-known intermediates during the catalytic oxidation of HCHO and are detected in the experiments. Four intense bands located at 2 914 ($ν(CH)$), 1 564 ($ν_{as}(COO^-)$), 1 415($δ(CH)$), and 1 340 ($ν_s(COO^-)$) cm^{-1} can be ascribed to the formate species [30, 31]. The intensity of the formate species bands on δ-MnO$_2$ and M-MnO$_2$ increased with the HCHO exposure time, suggesting that formate species accumulated gradually on the catalyst surface. Meanwhile, the pure δ-MnO$_2$ sample showed a much higher relative intensity of the formate species than M-MnO$_2$. According to the previous studies [28, 29], the catalytic performance of the catalysts decreased, with the formate species occupying the active sites of the catalysts. This can explain the gradual decrease in the catalytic performance of δ-MnO$_2$ over time. The decomposition of formate species is the governing process for HCHO oxidation at room temperature, and the formate species can be transformed to carbonate species by the surface hydroxyl groups [17]. The intensity of the negative and large band at 3533 cm^{-1} ($ν(OH)$) decreased gradually with the exposure time, indicating that the hydroxyl groups in the structure were continuously consumed during the reaction. Moreover, the carbonate species, located at 1 685 ($ν_{as}(CO_3)$) cm^{-1} and 1 201 ($ν_s(CO_3)$) cm^{-1}, were only found on M-MnO$_2$, as shown in Fig. 6c. These indicate that the decomposition efficiency of the formate species on M-MnO$_2$ is higher than on pure δ-MnO$_2$. It has been reported that hydroxyl groups play a key role in MnO$_2$-based catalysts and the surface hydroxyl groups can be regenerated by the reaction between surface active oxygen ($·O^-/·O_2^-$) and surface adsorbed water through the

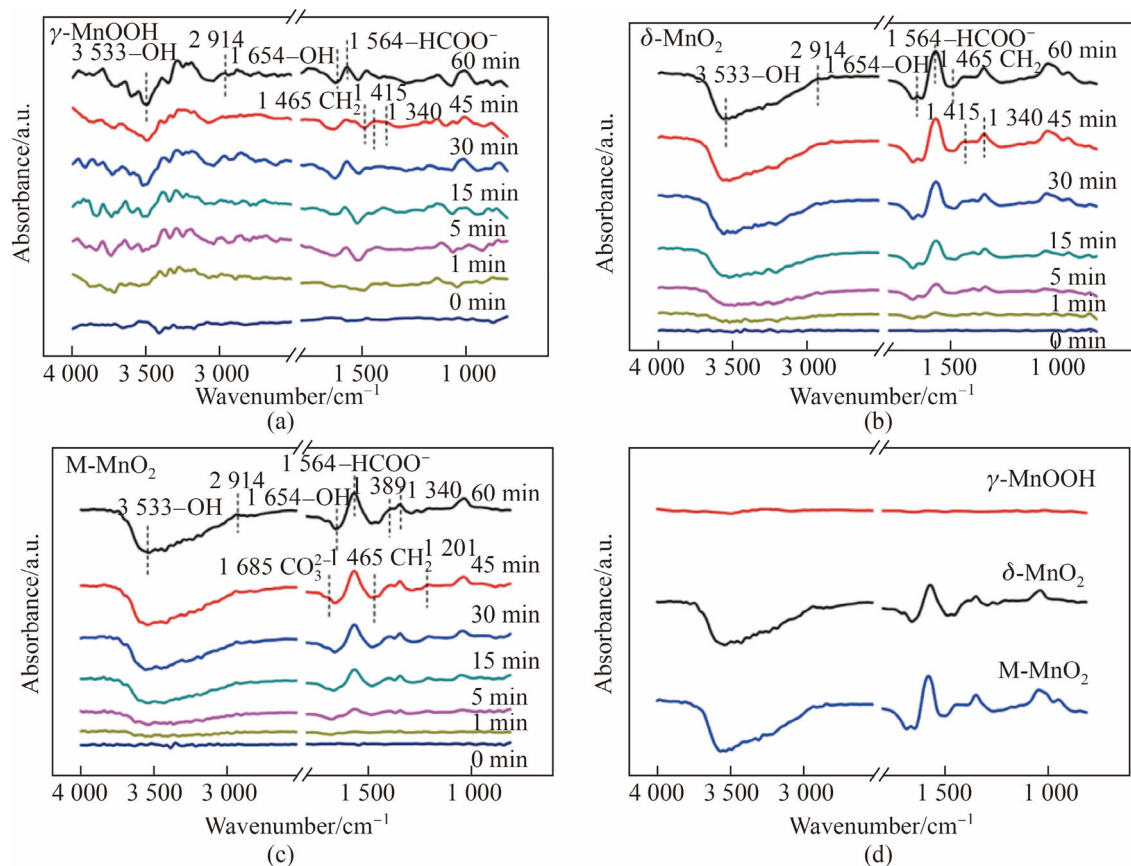**Fig. 6** In-situ DRIFTS spectra of **a** γ-MnOOH, **b** δ-MnO$_2$, **c** M-MnO$_2$ exposed to a flow of 80 mg/kg of HCHO/N$_2$ + 20% O$_2$/N$_2$ at room temperature and **d** high resolution of in-situ DRIFTS spectra of **a**–**c** at 60 min

reaction ($\cdot$O$^-$/$\cdot$O$_2^-$ + H$_2$O → 2-OH). The higher content of $\cdot$O$^-$/$\cdot$O$_2^-$ and surface adsorbed water on M-MnO$_2$ inevitably leads to a higher catalyst efficiency.

Based on the previous analysis, the mechanism of HCHO oxidation over M-MnO$_2$ at room temperature can be described as shown in Fig. 7. Normally, HCHO is oxidized by active oxygen ($\cdot$O$^-$/$\cdot$O$_2^-$) into DOM and

formate species after adsorbing on the catalyst surface, while the formate species tend to deposit on the catalyst surface, which requires more energy or surface hydroxyl groups to decompose. However, M-MnO$_2$ is composed of δ-MnO$_2$ nanosheets dispersed on γ-MnOOH nanowires, and this structure can be beneficial for the surface active oxygen compared with δ-MnO$_2$. According to the above-
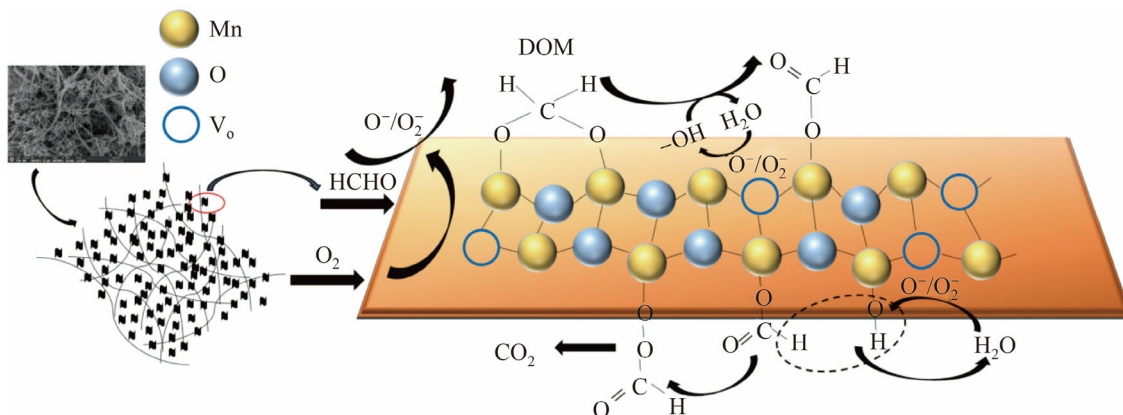

Fig. 7 Mechanism of HCHO oxidation over M-MnO$_2$ at room temperature

described experiments, the enhanced performance results from the special interconnected network structure, the dispersion and specific surface area of M-MnO$_2$ are clear. This special morphology can provide more surface active oxygen species, more surface adsorbed water, and thus, higher surface hydroxyl groups. Therefore, the formate species can be rapidly transformed to carbonate species and then decomposed to CO$_2$ and H$_2$O.

4 Conclusions

A special interconnected network structure, M-MnO$_2$, composed of δ-MnO$_2$ nanosheets and γ-MnOOH nanowires for HCHO oxidation was prepared by a facile one-step hydrothermal method. The obtained M-MnO$_2$ exhibited high catalytic activity, which reached 50% for 100 mg/kg HCHO oxidation for 10 h under a gas hourly space velocity (GHSV = 60 000 mL/(g$_{cat}$·h) higher than that of pure δ-MnO$_2$ nanosheets. It was found that the interconnected network structure provided sufficient surface active oxygen species and surface adsorbed water, resulting in excellent catalytic activity and stability for HCHO oxidation at room temperature. Moreover, the synthetic method is simple and can be easily implemented for large-scale industrial application.

References

1. Li J, Zhang P, Wang J et al (2016) Birnessite-type manganese oxide on granular activated carbon for formaldehyde removal at room temperature. J Phys Chem C 120(42):24121–24129
2. Salthammer T, Mentese S, Marutzky R (2010) Formaldehyde in the indoor environment. Chem Rev 110(4):2536–2572
3. Tang X, Bai Y, Duong A et al (2009) Formaldehyde in China: production, consumption, exposure levels, and health effects. Environ Int 35(8):1210–1224
4. Silbergeld E, Patrick T (2005) Environmental exposures, toxicologic mechanisms, and adverse pregnancy outcomes. Am J Obstet Gynecol 192(5):S11–S21
5. Grafstrom R, Fornace A, Autrup H et al (1983) Formaldehyde damage to DNA and inhibition of DNA repair in human bronchial cells. Science 220(4593):216–218
6. Emri G, Schaefer D, Held B (2004) Low concentrations of formaldehyde induce DNA damage and delay DNA repair after UV irradiation in human skin cells. Exp Dermatol 13(5):305–315
7. Bai B, Qiao Q, Li J et al (2016) Progress in research on catalysts for catalytic oxidation of formaldehyde. Chin J Catal 37(1):102–122
8. Yu B, He W, Li N et al (2016) Thermal catalytic oxidation performance study of swtco system for the degradation of indoor formaldehyde: kinetics and feasibility analysis. Build Environ 108:183–193
9. Torres J, Royer S, Bellat J et al (2013) Formaldehyde: catalytic oxidation as a promising soft way of elimination. ChemSus Chem 6(4):578–592
10. Guo J, Lin C, Jiang C et al (2019) Review on noble metal-based catalysts for formaldehyde oxidation at room temperature. Appl Surf Sci 475:237–255
11. Tang X, Chen J, Huang X et al (2008) Pt/MnO$_x$-CeO$_2$ catalysts for the complete oxidation of formaldehyde at ambient temperature. Appl Catal B Environ 81:115–121
12. Ye R, Wang X, Price C et al (2020) Engineering of yolk/core–shell structured nanoreactors for thermal hydrogenations. Small 16:1906250
13. Zhang C, He H (2007) A comparative study of TiO$_2$ supported noble metal catalysts for the oxidation of formaldehyde at room temperature. Catal Today 126(3):345–350
14. Quiroz J, Giraudon J, Gervasini A et al (2015) Total oxidation of formaldehyde over MnO$_x$-CeO$_2$ catalysts: the effect of acid treatment. ACS Catal 5(4):2260–2269
15. Liu P, He H, Wei G et al (2016) Effect of Mn substitution on the promoted formaldehyde oxidation over spinel ferrite: catalyst characterization, performance and reaction mechanism. Appl Catal B Environ 182:476–484
16. Boyjoo Y, Wang M, Pareek V et al (2016) Synthesis and applications of porous non-silica metal oxide submicrospheres. Chem Soc Rev 45(21):6013–6047
17. Wang J, Zhang P, Li J (2015) Room-temperature oxidation of formaldehyde by layered manganese oxide: effect of water. Environ Sci Technol 49(20):12372–12379
18. Chen S, Liu G, Yadegari H (2015) Three-dimensional MnO$_2$ ultrathin nanosheet aerogels for high-performance Li-O$_2$ batteries. J Mater Chem A 3(6):2559–2563
19. Morales M, Barbero B, Cadús L (2006) Total oxidation of ethanol and propane over Mn-Cu mixed oxide catalysts. Appl Catal B Environ 67:229–236
20. Liu F, Rong S, Zhang P et al (2018) One-step synthesis of nanocarbon-decorated MnO$_2$ with superior activity for indoor formaldehyde removal at room temperature. Appl Catal B Environ 235:158–167
21. Sekine Y, Nishimura A (2001) Removal of formaldehyde from indoor air by passive type air-cleaning materials. Atmos Environ 35(11):2001–2007
22. Wang J, Li J, Jiang C et al (2017) The effect of manganese vacancy in birnessite-type MnO$_2$ on room-temperature oxidation of formaldehyde in air. Appl Cataly B Environ 204:147–155
23. Chen T, Dou H, Li X et al (2009) Tunnel structure effect of manganese oxides in complete oxidation of formaldehyde. Microporous Mesoporous Mater 122(1):270–274
24. Chen H, He J, Zhang C et al (2007) Self-assembly of novel mesoporous manganese oxide nanostructures and their

application in oxidative decomposition of formaldehyde. J Phys Chem C 111(49):18033–18038

25. Zhang J, Li Y, Wang L et al (2015) Catalytic oxidation of formaldehyde over manganese oxides with different crystal structures. Catal Sci Technol 5(4):2305–2313

26. Selvakumar S, Nuns N, Trentesaux M et al (2018) Reaction of formaldehyde over birnessite catalyst: a combined XPS and ToF-SIMS study. Appl Catal B Environ 223:192–200

27. Wang J, Li D, Li P et al (2015) Layered manganese oxides for formaldehyde-oxidation at room temperature: the effect of interlayer cations. RSC Adv 5(122):100434–100442

28. Wu S, Chen W, Yan L (2014) Fabrication of a 3D MnO_2/graphene hydrogel for high-performance asymmetric supercapacitors. J Mater Chem A 2(8):2765–2772

29. Ye J, Zhou M, Le Y et al (2020) Three-dimensional carbon foam supported MnO_2/Pt for rapid capture and catalytic oxidation of formaldehyde at room temperature. Appl Catal B Environ 267:118689. https://doi.org/10.1016/j.apcatb.2020.118689

30. Rong S, Zhang P, Yang Y et al (2017) MnO_2 framework for instantaneous mineralization of carcinogenic airborne formaldehyde at room temperature. ACS Catal 7(2):1057–1067

31. Rong S, He T, Zhang P (2020) Self-assembly of MnO_2 nanostructures into high purity three-dimensional framework for high efficiency formaldehyde mineralization. Appl Cataly B Environ 267:118375. https://doi.org/10.1016/j.apcatb.2019.118375

32. Ramstedt M, Sjöberg S (2005) Phase transformations and proton promoted dissolution of hydrous manganite (gama-MnOOH). Aquat Geochem 11(4):413–431

33. Jia J, Zhang P, Chen L (2016) Catalytic decomposition of gaseous ozone over manganese dioxides with different crystal structures. Appl Cataly B Environ 189:210–218

34. Setvin M, Aschauer U, Scheiber P et al (2013) Reaction of O_2 with subsurface oxygen vacancies on TiO_2 anatase (101). Science 341(6149):988–991

35. Zhu L, Wang J, Rong S et al (2017) Cerium modified birnessite-type MnO_2 for gaseous Formaldehyde oxidation at low temperature. Appl Cataly B Environ 211:212–221

36. Peng X, Guo Y, Yin Q et al (2017) Double-exchange effect in two-dimensional MnO_2 nanomaterials. J Am Chem Soc 139(14):5242–5248

Ying Tao is a master degree student at Shanghai University. She received the master degree in 2019. Her research primarily focuses on catalytic and energy-saving material.
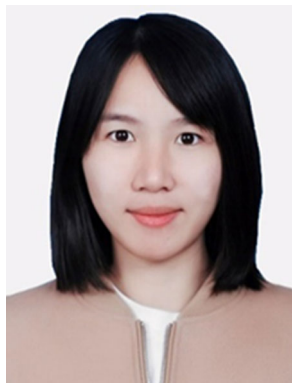
Rong Li is an Assistant Researcher at Shanghai Institute of Ceramics, Chinese Academy of Science. She received her maser degree from Shanghai Institute of Ceramics in 2013. She is mainly engaged in the research of nanotechnology and energy-saving materials.

Ai-Bin Huang is an Assistant Researcher at Shanghai Institute of Ceramics, Chinese Academy of Science. He received his doctor's degree from Shanghai Institute of Ceramics in 2017. He is mainly engaged in the research of chromatic materials for energy saving.

Yi-Ning Ma is an associate professor at Jiangsu Police Institute. He received his doctor's degree from Shanghai Institute of Ceramics in 2018. He is mainly engaged in the research of energy storage and latent fingerprint detection.

Shi-Dong Ji is a professor at shanghai university. He received his doctor's degree from Nagoya Institute of Technology in 2011. He is mainly engaged in the research of energy-saving materials.

Ping Jin is the Director of Research Center for Industrial Ceramics, Shanghai Institute of Ceramics, Chinese Academy of Science. He received his doctor's degree from Nagoya Institute of Technology in 1992. He is mainly engaged in the research of energy-saving materials.

Hong-Jie Luo is a professor at shanghai university. He received his doctor's degree from shanghai institute of ceramics in 1991. He was supported by China National Science Fund for Distinguished Young Scholars and the one-hundred-talent program of CAS. He is mainly engaged in the research of cultural relics conservation and energy-saving materials.